# Fast Fourier Transform–Based Analysis of Second-Harmonic Generation Image in Keratoconic Cornea

*Wen Lo,*[1,2,7] *Wei-Liang Chen,*[2,7] *Chiu-Mei Hsueh,*[2] *Ara A. Ghazaryan,*[2] *Shean-Jen Chen,*[1] *David Hui-Kang Ma,*[3] *Chen-Yuan Dong,*[*2,4,5] *and Hsin-Yuan Tan*[*,3,6]

**Purpose.** To qualify and quantify structural alterations in keratoconic corneas ex vivo by the use of second-harmonic generation (SHG) microscopy and two-dimensional fast Fourier transform (2D-FFT) analysis.

**Methods.** Two keratoconic and three normal human corneal specimens were imaged with a multiphoton microscope. Forward and backward second-harmonic generation images (FSHG and BSHG) of corneal stroma were obtained at high resolution and at different depths. The SHG images were further analyzed with a 2D-FFT algorithm to quantify the texture and orientation changes of collagen fibers.

**Results.** The results showed that the abnormality of collagen architecture was found through the whole layer of stroma. 2D-FFT analysis of SHG cornea images provided fiber orientation direction and an aspect ratio (AR) as a quantitative measure of fiber direction determination. It was found that for keratoconic cornea the average AR values are statistically greater than those of the normal cornea: 1.66 ± 0.42 (Case I keratoconic cornea), 1.72 ± 0.44 (Case II keratoconic cornea), and 1.34 ± 0.16 (average of three normal human corneas). Furthermore, the fiber directions determined by 2D-FFT analysis of BSHG and FSHG images were strongly correlated for large AR values (AR > 2).

**Conclusions.** The high correlation between FSHG and BSHG fiber direction for large AR values shows that BSHG imaging can provide qualitative and quantitative information of the extent of structural changes in a keratoconic cornea. The ability to use BSHG for diagnosing and monitoring stroma abnormalities, even when cornea transparency is retained, demonstrates the clinical potential of this method. (*Invest Ophthalmol Vis Sci.* 2012;53:3501–3507) DOI:10.1167/iovs.10-6697

From the [1]Department of Engineering Science, National Cheng Kung University, Tainan, Taiwan; the [2]Department of Physics, National Taiwan University, Taipei, Taiwan; the [3]Department of Ophthalmology, Chang Gung Memorial Hospital, College of Medicine, Chang Gung University, Linko, Taiwan; the [4]Center for Quantum Science and Engineering, National Taiwan University, Taipei, Taiwan; the [5]Biomedical Molecular Imaging Core, Research Center for Medical Excellence, Division of Genomic Medicine, National Taiwan University, Taipei, Taiwan; and the [6]Institute of Biomedical Engineering, National Taiwan University, Taipei, Taiwan.

Supported by National Science Council (NSC 99-2221-E-002-096-MY3, 99-2221-E-002-096-MY3) in Taiwan, National Health Research Institute (NHRI) (NHRI-EX100-10041EI) in Taiwan, National Taiwan University (NTU-99R70409), Center for Quantum Science and Engineering, National Taiwan University (CQSE-99R80870), and Chang Gung Memorial Hospital (CMRP350841-4).

[7]These authors contributed equally to the work presented here and should therefore be regarded as equivalent authors.

Submitted for publication October 8, 2010; revised July 29, 2011, February 22 and March 22, 2012; accepted April 24, 2012.

Disclosure: **W. Lo**, None; **W.-L. Chen**, None; **C.-M. Hsueh**, None; **A.A. Ghazaryan**, None; **S.-J. Chen**, None; **D.H.-K. Ma**, None; **C.-Y. Dong**, None; **H.-Y. Tan**, None

*Each of the following is a corresponding author: Hsin-Yuan Tan, Department of Ophthalmology, Chang Gung Memorial Hospital, College of Medicine, Chang Gung University, Linko 333, Taiwan; b0401018@cgmh.org.tw.

Chen-Yuan Dong, Department of Physics, National Taiwan University, Taipei 106, Taiwan; cydong@phys.ntu.edu.tw.

Multiphoton microscopy (MPM) is an emerging technique that has been widely applied in the field of biomedicine. Using a near-infrared light source, MPM has advantages of increased imaging depth, intrinsic optical sectioning, and reduced photodamage that enables effective biological imaging at the microscopic scale to be performed.[1] This imaging modality has been applied successfully for visualizing physiologic and pathologic changes in many biological organs/tissue, including skin, liver, and lung.[2–4] In ophthalmology, the cornea is one of the ideal target organs for MPM imaging for its characteristics of high transparency, high structural percentage of collagen, and the outermost localization that makes noninvasive in vivo imaging possible. Many have successfully demonstrated the feasibility of MPM in corneal imaging.[5–8] In particular, two-photon excited autofluorescence was used either to monitor the metabolic activities of cellular components or to visualize the presence of pathogens within the cornea.[9,10] Second-harmonic generation (SHG) signal, a nonlinear optical effect derived from noncentrosymmetric structures such as collagen, provided useful structural information from corneal stroma that is composed mainly of type I collagen.[11] However, unlike any other tissues, a significant discrepancy between forward-propagating and backward-propagating SHG (FSHG and BSHG) images was noted in normal transparent corneal stroma.[6,8] FSHG signals showed the collagenous fibrillar structures within transparent corneas, whereas BSHG signals were much weaker and provided only an obscure outline of collagenous lamellae organization. A proposed explanation of the discrepancy between FSHG and BSHG images is the greatly reduced backscattering effect within a transparent cornea.[6] Nevertheless, a general outline of lamellae bundle was observed within large-area BSHG images in normal and keratoconic corneas, whereas this particular pathology preserved transparency to a variable degree.[7,8,12,13] Therefore, in this work, we applied the two-dimensional fast Fourier transform (2D-FFT) algorithm for analyzing the correlations between FSHG and BSHG images in keratoconic corneas, to reinvestigate the potentials and clinical feasibility of BSHG imaging in transparent corneas.

## Methods

### SHG Microscope

SHG imaging was performed on a custom-modified laser scanning microscope similar to ones described previously.[7,13–16] The 780-nm

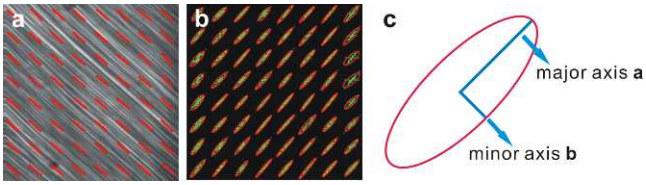


**Figure 1.** (**a**) BSHG image of rat tail tendon in grayscale. The overlapped red lines demonstrate the fiber direction determined by 2D-FFT analysis. (**b**) 2D-FFT images within the 8 × 8 domains. Each red ellipse represents fitting of the 2D-FFT pattern to the elliptical model. (**c**) The elliptical model used in fitting the 2D-FFT patterns.

output of a titanium–sapphire laser (Tsunami; Spectra Physics, Mountain View, CA) was guided into an upright microscope. Two commercial microscopes (Olympus BX51; Olympus, Tokyo, Japan and a Nikon E800; Nikon, Tokyo, Japan) were used in this study. The laser light was reflected by the main dichroic mirror (700dcspruv-3p; Chroma Technology, Rockingham, VT) before it was focused onto the specimens with a long working distance water-immersion objective (XLUMPFLN ×20 W NA 0.95; Olympus). The same objective collects the 390-nm BSHG signals, which then passed through the main dichroic mirror, and are further selected by a secondary dichroic mirror and two band-pass filters (435DCXR and HQ390/20; Chroma Technology). A single photon counting photomultiplier tube (PMT) (R7400P; Hamamatsu, Hamamatsu City, Japan) records the signal. For FSHG signal detection, a tube lens was used for signal collection, and further separated by the same combination of dichroic mirror and band-pass filter as the BSHG detection. The FSHG signal was recorded by a PMT module (R5700P; Hamamatsu). A motorized sample stage controlled by the computer allows large-area tile scanning. The acquisition time for a single 256 × 256 pixel image covering 110 ×110 $\mu m^2$ is approximately 4 to 5 seconds. For large-area tile scanning, additional time is spent on the movement of the motorized stage. For example, the time to acquire a 5.5 × 5.5 $mm^2$ image is approximately 5 hours.

## Specimen Preparation

Two specimens from partially excised keratoconic corneal buttons were obtained for SHG imaging during scheduled surgeries of penetrating keratoplasty. Slit-lamp examination found no significant scar in the Case I cornea and a central scar in the Case II cornea. For comparison, a discarded normal corneal specimen (Normal cornea I) composed of the anterior half of a stroma dissected by microkeratome (Moria Inc., Doylestown, PA) with a 350-μm head during routine endothelial keratoplasty, and two normal human corneas (Normal corneas II and III) not suitable for transplantation were obtained from a tissue bank (Minnesota Lions Eye Bank, Saint Paul, MN). Prior to multiphoton examination, corneal specimens were stored in 20% dextran (dextran T500; Pharmacosmos, Holbaek, Denmark) PBS

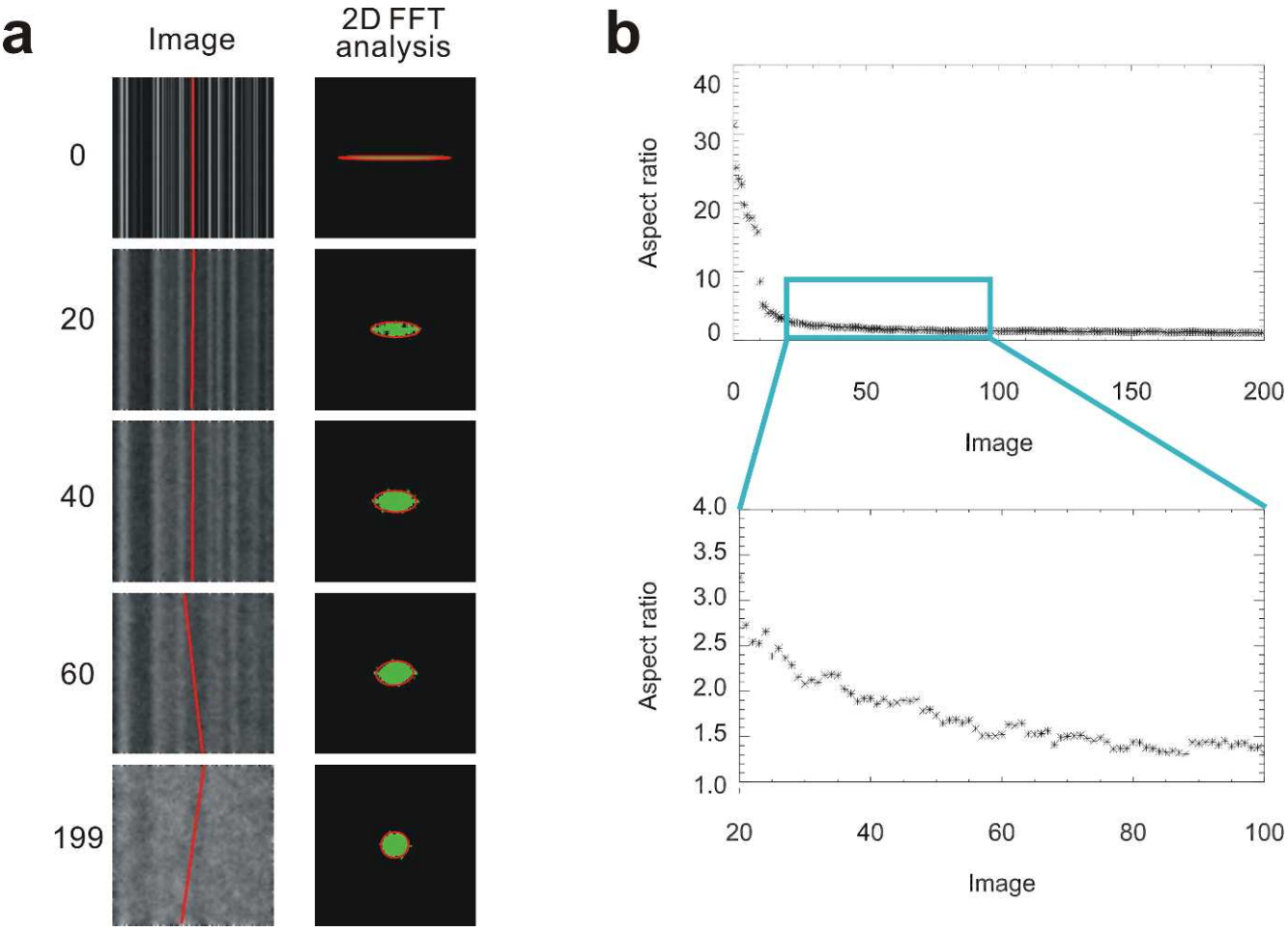


**Figure 2.** Simulation showing the identification of fiber direction by 2D-FFT analysis. (**a**) Simulated fiber pattern with successive increase of pattern randomization. Image 0 represents the image with clear fiber texture. The *red lines* indicate directions of the image patterns as determined from 2D-FFT analysis. Successive iteration of image randomization led to increasingly blurry fibril patterns. (**b**) Plot showing decrease in aspect ratio with increased randomization iterations.

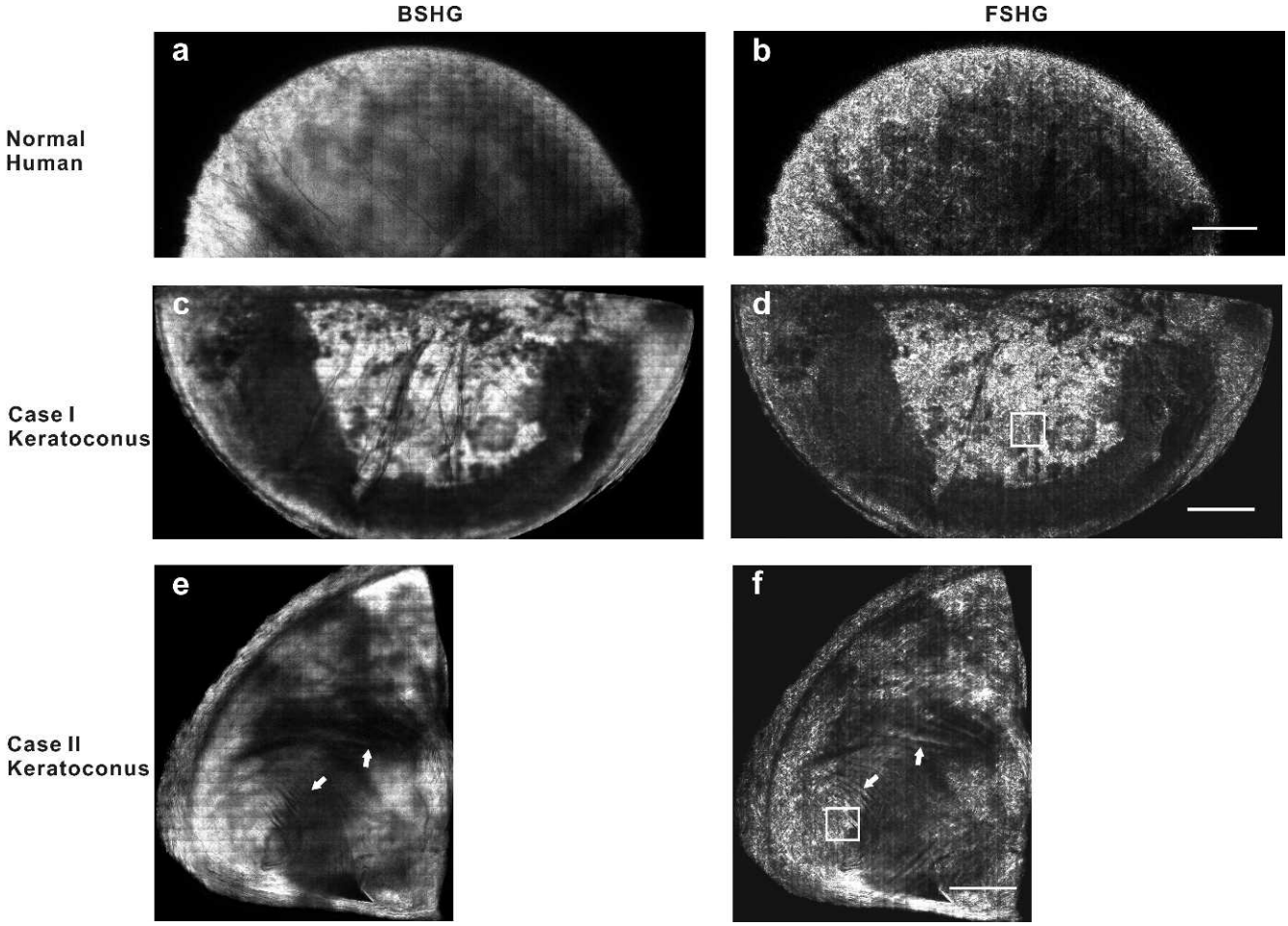


**Figure 3.** BSHG (**a**, **c**, **e**) and FSHG (**b**, **d**, **f**) images of the normal human cornea and the two cases of keratoconus corneas acquired at the depth of 200 μm. 2D-FFT analysis of the white boxed region in (**d**) and (**f**) are shown in Figure 4. Scale bar: 1 mm.

solution to avoid excess swelling. The specimens were then sealed in glass well slides and mounted on the microscope for imaging.

To analyze the fiber orientation in FSHG and BSHG images, the 2D-FFT algorithm was used in the postprocessing of acquired images, implemented through a custom-developed scientific multidiscipline programming language (IDL 6.4; ITT Visual Information Solutions, Boulder, CO) program.

## Results

### Determination of Fiber Orientation from 2D-FFT Analysis

Figure 1 shows a demonstration of our 2D-FFT analysis in determining the fiber direction of a rat tail tendon specimen. Specifically, Figure 1a is the grayscale BSHG image of a rat tail tendon. For 2D-FFT analysis, the image was first divided into equally sized domains. The smaller the domain size, the better is the ability of 2D-FFT analysis to differentiate the fiber directional changes within the image. However, a domain size that is too small displays an insufficient amount of fiber morphology for accurate determination of fiber direction by 2D-FFT analysis. Since the BSHG image of a rat tail tendon reveals a fairly uniform distribution of collagen fiber orientations (Fig. 1a), we have divided the image into $8 \times 8$ domains, although a smaller domain could have been chosen. In this case, each domain is $32 \times 32$ pixels corresponding to an area of $14 \times 14$ $\mu m^2$. Next, 2D-FFT analysis was performed on each domain, and a threshold value was set to transform the 2D-FFT images into a pattern with magnitudes of 0 and 1 (green patterns in Fig. 1b), to delineate the contours of the 2D-FFT patterns. Quantification of the fiber geometry was performed by fitting the contour of the 2D-FFT image with an ellipse (red ellipses in Fig. 1b), and the aspect ratio (AR) of the fitted ellipse, defined as the ratio of the major and minor axes, was determined (Fig. 1c). The direction of the minor axis (red lines shown in Fig. 1a) corresponds to the direction of the tendon fiber.[17]

### Simulation Test of 2D-FFT Analysis for Fiber Direction

To demonstrate the ability of our approach to effectively predict the quality of fiber geometry, we artificially created a fibrous pattern in the vertical direction that was gradually blurred by repeated operations of randomization. In each successive operation, random numbers were introduced in 10% of the original image. Figure 2a shows the created fibrous pattern images and the corresponding 2D-FFT analysis. The vertical, fibrous images along with 20, 40, 60, and 199 image randomization operations are shown on the left column. The corresponding 2D-FFT patterns (green pseudocolor) and the fitted ellipses (red pseudocolor) of the fibrous images are shown on the right column of Figure 2a, with the original image displaying the most clear fibrous morphology. Increasing

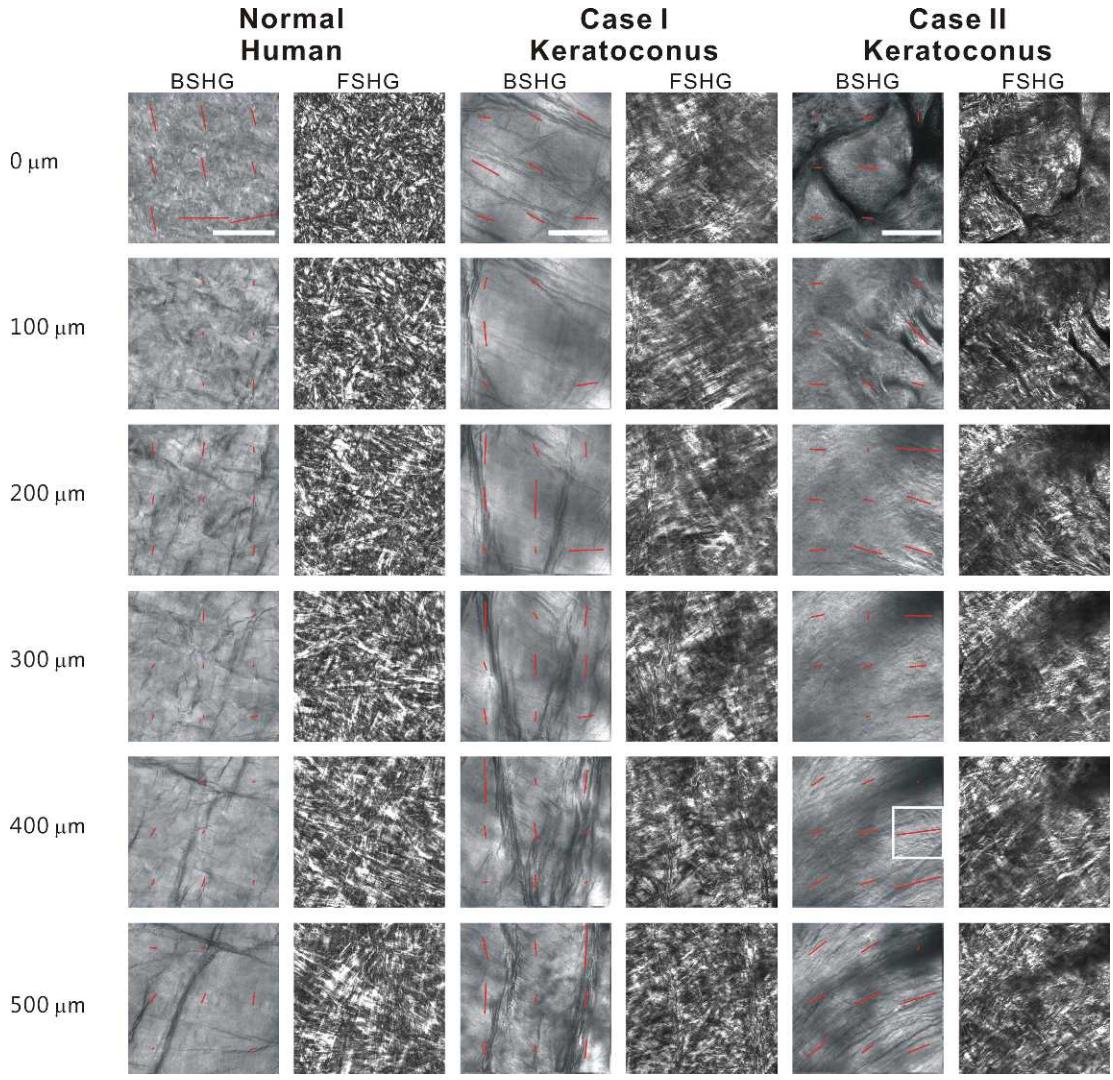


**Figure 4.** BSHG and FSHG images of normal human cornea and the two cases of keratoconus corneas at different depths. *Red lines* indicate the directions of fibrous structures determined from analyzable domains of BSHG images by 2D-FFT analysis (scale bar: 200 μm). The lengths of the *red lines* are scaled to the corresponding AR values. Magnified view of the white boxed region is shown in Figure 6.

iterations of randomization result in increasingly blurry images and gradual degeneration of the 2D-FFT pattern from a line shape to a round shape, indicating a loss of directionality in the image. The fiber directions determined from 2D-FFT analysis are then projected onto the fibrous patterns (red lines in left column). The morphologic changes in the 2D-FFT patterns were also quantified by calculating the ARs of the fitted ellipses, which approaches 1 with increasing numbers of image randomization. Figure 2b shows the decreasing trend of AR and its approach to the value of 1 as the fibril texture blurred. In the iteration 199 image, the fibril structure in the initial image is no longer apparent, and attempting to apply 2D-FFT analysis leads to a nonsensible result. Therefore, when AR values fall below 1.3, or when the 2D-FFT pattern cannot be fitted with an elliptical model, we consider the domain not analyzable.

## FSHG and BSHG Images of Keratoconic Corneas

To compare the morphologic features obtained from FSHG and BSHG images of the keratoconus specimens, large-area FSHG and BSHG images of normal human and keratoconus cornea specimens were obtained (Fig. 3). Frequent bundlelike structures are found in the BSHG image (arrow in Fig. 3e), which differs from the homogeneous pattern within a normal cornea (Fig. 3a). This result agrees with BSHG imaging of our earlier work[13] that observed an arced pattern appearing in the region near the presumed apex. Similar architecture is also observed in a corresponding FSHG image (arrow in Fig. 3f).

## 2D-FFT Analysis of FSHG and BSHG Images of Keratoconic Cornea

We further obtained depth-resolved images within the white boxed regions in Figures 3d and 3f and several areas in the normal cornea specimens, and analyzed the results by 2D-FFT algorithm. The resultant images are shown in Figure 4 together with that of a normal cornea for comparison. In Figure 4, BSHG images of the normal and keratoconic corneas are divided into $3 \times 3$ domains for 2D-FFT analysis, with the red lines representing the determined direction of the fibril texture orientation for the analyzable domains. The lengths of the red lines have also been scaled to the corresponding AR value to allow a visualization of the variations in the aspect ratio. The FSHG images of the corresponding area are shown in the

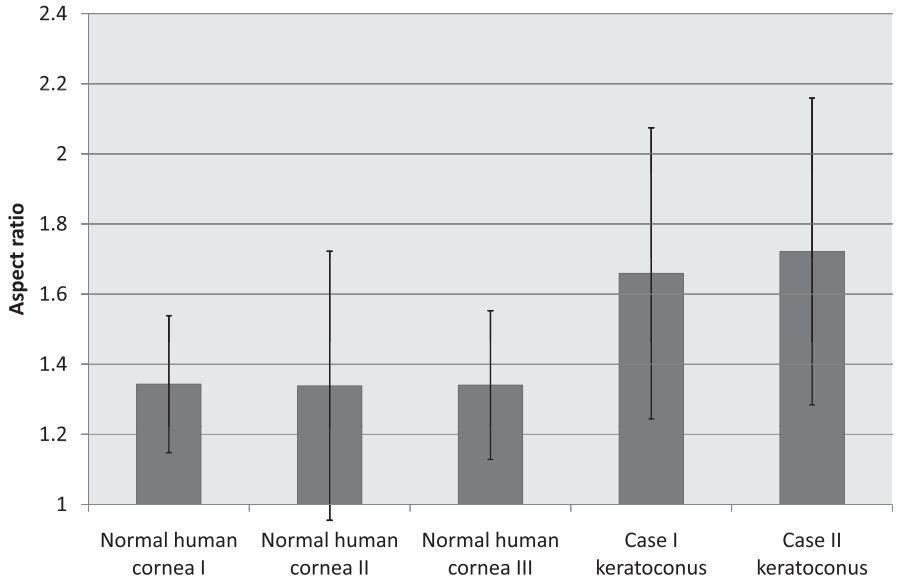


**Figure 5.** Averaged ARs in the three normal human corneas and the two cases of keratoconus corneas as determined from 2D-FFT analysis of the BSHG images.

adjacent column for comparison. For the normal human cornea, fibril-like patterns were not generally observed in the BSHG imaging, and 2D-FFT analysis of the BSHG images did not show a preferential direction (Fig. 4). However, 2D-FFT analysis of the selected regions of interest in both keratoconic specimens showed a preferential fiber direction (Fig. 4). This feature was observed in both the anterior (0–100 μm) and posterior stroma (400–500 μm).

In addition to fiber direction, we also determined the averaged values of the ARs from the BSHG images of normal and keratoconic corneas. The average for the three normal human corneas were found to be 1.34 ± 0.16, whereas the keratoconus cases I and II were found to be 1.66 ± 0.42 and 1.72 ± 0.44, respectively (Fig. 5). For Normal cornea I, the ARs were determined from 173 × 173 μm domains covering 1 × 1 mm area and three depths, whereas the ARs for Normal cornea II and cornea III were averaged using 163 × 163 μm domains covering 0.64 × 0.64 mm area and all depths shown in Figure 4. For the keratoconus corneas the AR averaging was performed using 190 × 190 μm domains covering 0.6 × 0.6 mm area and all depths shown in Figure 4. Six sample *t*-tests comparing the three normal samples with the two keratoconus samples were used to analyze whether AR values obtained in BSHG images can effectively differentiate structural alterations for keratoconic corneas from the normal human cornea. With more than 90 domains used in each comparison, results of the *t*-tests show that the AR values in keratoconus corneas are statistically ($P < 0.05$) higher than that of normal human cornea.

In addition, we found that when the AR of a BSHG image is >2, the correlation of fiber orientations determined from 2D-FFT analysis of both FSHG and BSHG image is high. An example of this feature is illustrated in Figure 6, where we show the BSHG and FSHG images of the selected region in Figure 4 (Case II keratoconus specimen, at the depth of 400 μm). We performed 2D-FFT analysis of the BSHG image as a single domain and displayed the derived fiber orientation in red. For the FSHG image that more clearly reveals the fibrous texture, we divided the image into 11 × 11 domains and performed 2D-FFT on each domain. The average angle derived from the analyzable domains of the FSHG image was 15.1 ± 14.1°, and the angle derived from the BSHG image was 7.5° measured counterclockwise from the horizontal. To examine the generality of this effect, we performed a similar analysis for all the FSHG and BSHG images of the Case II keratoconic cornea shown in Figure 4, and determined the Pearson product-moment correlation coefficient between the derived angles of BSHG domains and the average derived angles of the FSHG domains. We found that when the calculated BSHG AR value is >2, the average correlation coefficient has a highly correlated value of 0.95, whereas when the AR value is <1.5, the correlation coefficient is 0.48.

## Discussion

In this study, we used SHG microscopy and a 2D-FFT algorithm to analyze FSHG and BSHG images of ex vivo keratoconic corneas. In the large-area FSHG and BSHG images covering the entire specimens (Fig. 3), fibril patterns on the millimeter scale are observed in the two keratoconus cases. Large-area imaging of keratoconic corneas also suggests that structural alteration does not occur homogeneously in the corneal stroma. The localized collagen structural abnormality may account for the

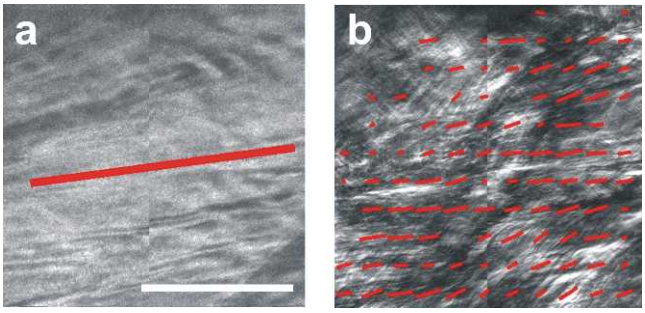


**Figure 6.** (**a**) BSHG image of the selected area in Figure 4 (AR value of 2.84). *Red line* shows the 2D-FFT–derived fiber direction with the whole image as a single domain. (**b**) FSHG image of the same area divided into 11 × 11 domains for 2D-FFT analysis (scale bar: 100 μm). The lengths of the *red lines* are scaled to the corresponding AR values. The similarity of the fiber direction in the BSHG and the FSHG image is visibly apparent.

structural weakness, the accompanied slippage[18] of the stromal lamella, and the corneal protrusion. Moreover, in-depth imaging shows that the fibril structure changes are observed not only in regions adjacent to Bowman's layer, as described in a previous study,[12] but also in the middle and posterior stroma.

Our results show that fiberlike patterns can be observed in BSHG images of keratoconus corneas. Quantitative 2D-FFT analysis verifies that BSHG imaging in keratoconus corneas displays more fibrous characteristics than those of a normal cornea. This phenomenon was quantified by calculating the AR. Our results show that even when there is no significant scar observed with the slit-lamp examination (Case I), increased fibril texture is observed in the BSHG imaging of keratoconus cornea with high AR. In addition, in a cornea with explicit fibril patterns in its BSHG image (AR $>$ 2), the fiber orientation in BSHG imaging is positively correlated to the average fiber direction in FSHG. A possible explanation for BSHG's capability to reveal fiber patterns in a keratoconic cornea is that the stromal remodeling following the disruption of the fiber direction crossings between adjacent lamella collagen fibrils results in more uniformly directed collagen fibrils between adjacent lamella layers.[19–21] Another possible explanation is that keratoconus corneas are often thinner than normal corneas, which may affect the contribution of the backscattered FSHG signal to the BSHG signal.[22] However, in our thin normal cornea sample (Normal cornea I) composed of only the anterior half of the stroma, we did not observe any increase in fibrous characteristics (Fig. 5), consistent with the other two normal thickness cornea samples.

Our results suggest that the ARs derived from quantitative 2D-FFT analysis of the BSHG images may be used as indicators of the progress of keratoconus. With suitable clinical arrangement, the methodology described in this work may be used as a qualitative and quantitative tool for diagnosing and monitoring cornea stroma abnormalities while the transparency is retained. Although the image acquisition speed of the scanning systems used in this study is too slow for practical clinical use, many techniques that significantly improve the image acquisition speed have been developed to address this issue. One method to increase the scanning rate is to replace the horizontal galvanometer scanners with a fast rotating polygonal mirror.[1,23,24] Another method is to use acoustic optical modulators in place of scanning mirrors for laser beam deflection, which not only increases the scanning speed but also performs random access scanning of multiple regions of interest.[25] The imaging acquisition rate has also been improved with multifocal scanning, which simultaneously scans multiple positions in an image.[26–28] Finally, the temporal focusing technique generates a signal over a large area of the imaging plane, allowing image acquisition at a greater speed than that of the conventional video rate.[29] Combining 2D-FFT analysis with a fast acquisition system, BSHG imaging of keratoconus may have the potential in clinical application as a noninvasive, effective diagnostic and monitoring system.

## *References*


1. So PTC, Dong C-Y, Masters BR, Berland KM. Two-photon excitation fluorescence microscopy. *Annu Rev Biomed Eng*. 2000;2:399–429.
2. Lin SJ, Jee SH, Kuo CJ, et al. Discrimination of basal cell carcinoma from normal dermal stroma by quantitative multiphoton imaging. *Opt Lett*. 2006;31:2756–2758.
3. Li FC, Liu Y, Huang GT, et al. In vivo dynamic metabolic imaging of obstructive cholestasis in mice. *Am J Physiol Gastrointest Liver Physiol*. 2009;296:G1091–G1097.
4. Wang C-C, Li F-C, Wu R-J, et al. Differentiation of normal and cancerous lung tissues by multiphoton imaging. *J Biomed Opt*. 2009;14:044034.
5. Yeh AT, Nassif N, Zoumi A, Tromberg BJ. Selective corneal imaging using combined second-harmonic generation and two-photon excited fluorescence. *Opt Lett*. 2002;27:2082–2084.
6. Han M, Giese G, Bille J. Second harmonic generation imaging of collagen fibrils in cornea and sclera. *Opt Express*. 2005;13:5791–5797.
7. Teng SW, Tan HY, Peng JL, et al. Multiphoton autofluorescence and second-harmonic generation imaging of the ex vivo porcine eye. *Invest Ophthalmol Vis Sci*. 2006;47:1216–1224.
8. Morishige N, Petroll WM, Nishida T, Kenney MC, Jester JV. Noninvasive corneal stromal collagen imaging using two-photon-generated second-harmonic signals. *J Cataract Refract Surg*. 2006;32:1784–1791.
9. Piston DW, Masters BR, Webb WW. 3-Dimensionally resolved Nad(P)H cellular metabolic redox imaging of the in-situ cornea with 2-photon excitation laser-scanning microscopy. *J Microsc*. 1995;178:20–27.
10. Tan HY, Sun Y, Lo W, et al. Multiphoton fluorescence and second harmonic generation microscopy for imaging infectious keratitis. *J Biomed Opt*. 2007;12:024013.
11. Zipfel WR, Williams RM, Webb WW. Nonlinear magic: multiphoton microscopy in the biosciences. *Nat Biotechnol*. 2003;21:1368–1376.
12. Morishige N, Wahlert AJ, Kenney MC, et al. Second-harmonic imaging microscopy of normal human and keratoconus cornea. *Invest Ophthalmol Vis Sci*. 2007;48:1087–1094.
13. Tan HY, Sun Y, Lo W, et al. Multiphoton fluorescence and second harmonic generation imaging of the structural alterations in keratoconus ex vivo. *Invest Ophthalmol Vis Sci*. 2006;47:5251–5259.
14. Lo W, Teng SW, Tan HY, et al. Intact corneal stroma visualization of GFP mouse revealed by multiphoton imaging. *Microsc Res Tech*. 2006;69:973–975.
15. Lo W, Chang YL, Liu JS, et al. Multimodal, multiphoton microscopy and image correlation analysis for characterizing corneal thermal damage. *J Biomed Opt*. 2009;14:054003.
16. Wang TJ, Lo W, Hsueh CM, Hsieh MS, Dong CY, Hu FR. Ex vivo multiphoton analysis of rabbit corneal wound healing following conductive keratoplasty. *J Biomed Opt*. 2008;13:034019.
17. Matteini P, Ratto F, Rossi F, et al. Photothermally-induced disordered patterns of corneal collagen revealed by SHG imaging. *Opt Express*. 2009;17:4868–4878.
18. Polack FM. Contributions of electron microscopy to the study of corneal pathology. *Surv Ophthalmol*. 1976;20:375–414.
19. Meek KM, Tuft SJ, Huang YF, et al. Changes in collagen orientation and distribution in keratoconus corneas. *Invest Ophthalmol Vis Sci*. 2005;46:1948–1956.
20. Han M, Giese G, Bille JF. Second harmonic generation imaging of collagen fibrils in cornea and sclera. *Opt Express*. 2005;13:5791–5797.
21. Hayes S, Boote C, Tuft SJ, Quantock AJ, Meek KM. A study of corneal thickness, shape and collagen organisation in keratoconus using videokeratography and X-ray scattering techniques. *Exp Eye Res*. 2007;84:423–434.
22. Legare F, Pfeffer C, Olsen BR. The role of backscattering in SHG tissue imaging. *Biophys J*. 2007;93:1312–1320.
23. Kim P, Puoris'haag M, Côté D, Lin CP, Yun SH. In vivo confocal and multiphoton microendoscopy. *J Biomed Opt*. 2008;13:010501.
24. Kim KH, Buehler C, So PTC. High-speed, two-photon scanning microscope. *Appl Optics*. 1999;38:6004–6009.

25. Salome R, Kremer Y, Dieudonne S, et al. Ultrafast random-access scanning in two-photon microscopy using acousto-optic deflectors. *J Neurosci Methods*. 2006;154:161–174.
26. Straub M, Lodemann P, Holroyd P, Jahn R, Hell SW. Live cell imaging by multifocal multiphoton microscopy. *Eur J Cell Biol*. 2000;79:726–734.
27. Hell SW, Andresen V. Space-multiplexed multifocal nonlinear microscopy. *J Microsc*. 2001;202:457–463.
28. Bewersdorf J, Pick R, Hell SW. Multifocal multiphoton microscopy. *Opt Lett*. 1998;23:655–657.
29. Oron D, Tal E, Silberberg Y. Scanningless depth-resolved microscopy. *Opt Express*. 2005;13:1468–1476.